Materials & Design 254 (2025) 114016

Contents lists available at ScienceDirect

Materials & Design

journal homepage: www.elsevier.com/locate/matdes

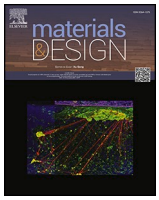

Graded SiC reinforced magnesium wires: Towards high throughput composite alloy discovery

Zhuocheng Xu [a,g], Xingjian Zhao [b], Oliver Watts [c], W. Mark Rainforth [d], Milo S.P. Shaffer [e,f,*], Sam Holdsworth [c], Dikai Guan [b,*], Qianqian Li [a,*]

[a] Department of Aeronautics, Imperial College London, London SW7 2AZ, United Kingdom
[b] Department of Mechanical Engineering, University of Southampton, Southampton SO17 1BJ, United Kingdom
[c] TWI Ltd., Granta Park, Great Abington, Cambridge CB21 6AL, United Kingdom
[d] School of Chemical, Materials and Biological Engineering, University of Sheffield, Sheffield S1 3JD, United Kingdom
[e] Department of Materials, Imperial College London, South Kensington Campus, London SW7 2AZ, United Kingdom
[f] Department of Chemistry, Molecular Sciences Research Hub (MSRH), Imperial College London, 82 Wood Lane, London W12 0BZ, United Kingdom
[g] Department of Mechanical Engineering, Imperial College London, London SW7 2AZ, United Kingdom

ARTICLE INFO

Keywords:
High-throughput prototyping
SiC reinforced Mg matrix composite
Graded composite
Stationary-shoulder friction stir channelling (SS-FSC)

ABSTRACT

High-throughput methods can accelerate the development of metal alloys and (nano)composites, both empirically and as input to computational methods. This study introduces a new route to fabricating composite wires with longitudinally varying composition using the byproduct of stationary-shoulder friction stir channelling (SS-FSC); this sample format is attractive for a variety of rapid read-out options in the future. The concept is illustrated by preparing Mg composite wires with a longitudinally graded concentration of SiC-particles. Spark plasma sintering (SPS) was used to encode a step-change in SiC concentration within a feedstock billet. Subsequent SS-FSC transformed this discrete compositional step into a continuous, graded extruded wire. Microstructural analysis revealed significant grain refinement from the SPS billet (44.3 ± 2.3 μm) to the SS-FSC wire (7.4 ± 0.5 μm), with even finer grains in SiC-loaded regions (5.1 ± 0.5 μm), attributed to particle-stimulated nucleation. Mechanical characterisation confirmed a hardness increase, from 65.8 ± 1.2 HV3 to 68.9 ± 2.7 HV3 (high SiC-content). This proof-of-concept study confirms the effectiveness of SS-FSC in producing high-quality wires with tailored microstructural and mechanical gradients. Additional compositions could be readily multiplexed in the original billet, providing a robust high-throughput technique for comprehensive structure–property investigations of advanced alloys and composites.

1. Introduction

Mg and Al alloys, as well as their metal matrix composites (Mg/Al-MMCs), are promising candidates as next-generation lightweight structural materials for aeronautic and automotive applications due to their high specific strength and cost efficiency [1–6]. However, current alloy and composite development approaches often rely on traditional Design of Experiments (DOE) methods, which are time-consuming and cost-inefficient, limiting the rapid iteration and advancement of novel lightweight alloys and composites. Therefore, introducing high-throughput methods capable of rapidly determining correlations between compositional/microstructural features and material properties has become increasingly essential. Such methods facilitate extensive experimental validation, providing valuable data for direct comparisons with theoretical simulations [7,8], and may ultimately facilitate real-time, Bayesian, or machine learning driven, optimisation and exploration.

Currently, various methods introducing compositional and/or microstructural gradients within alloys and composites have been explored [9–22]. For instance, the rapid alloy prototyping (RAP) approach, involving bulk casting, rolling, and heat treatment, has been employed to investigate the effects of Al weight fraction on the microstructural and mechanical properties of Fe–Mn alloys [23]. However, the discrete compositional gradients produced by this approach hinder the continuous evaluation of alloy properties.

Previous studies have employed techniques such as friction stir

* Corresponding authors.
E-mail addresses: m.shaffer@imperial.ac.uk (M.S.P. Shaffer), dikai.guan@soton.ac.uk (D. Guan), qianqian.li@imperial.ac.uk (Q. Li).

https://doi.org/10.1016/j.matdes.2025.114016
Received 13 February 2025; Received in revised form 6 April 2025; Accepted 26 April 2025
Available online 28 April 2025

processing (FSP) and its derivatives [11,24–26], gradient sintering [12], centrifugal casting [20,27], laser-based additive manufacturing [13–15,28], thin film deposition [16–18,29] and diffusion couple to create continuous gradients in composition and microstructure within alloy and composite samples. In the context of Mg/Al-MMCs, prior attempts to produce graded compositions involved centrifugal casting [20,27] and frictional stir extrusion [21]. Nevertheless, these methods typically produce tubular samples with radial, poorly controlled gradients, limiting their practical application for high-throughput material discovery.

Friction stir welding (FSW) and its derivative, friction stir processing (FSP), are solid-state techniques enabling mechanical mixing and atomic-scale diffusion within stirred materials. In previous studies, FSP, particularly friction stir vibration processing (FSVP), which introduces vibrations perpendicular to the processing direction, has been successfully employed to fabricate Mg/Al matrix surface composites with homogeneous reinforcement distributions [30–32]. This capability to achieve homogeneous mixing makes these methods ideal candidates for high-throughput composite fabrication. Indeed, a previous investigation successfully demonstrated the creation of a continuous Al concentration gradient by applying FSP between adjacent AZ91 and AZ31 alloy plates [25]. We hypothesise that a similar approach could generate a longitudinal compositional gradient within Mg/Al-MMCs, allowing each position along the processed sample to exhibit a specific, well-defined composition suitable for comprehensive cross-correlated characterisation.

Stationary-shoulder friction stir channelling (SS-FSC), also known as CoreFlow®, is a subsurface channelling technique developed by The Welding Institute (TWI), leveraging friction stir mechanisms. Initially designed to create internal structures within finished components (e.g., heat sinks), SS-FSC also generates wire-shaped by-products. We have previously demonstrated that these wires exhibit microstructural modifications similar to conventional FSP-treated Mg/Al alloys, including grain refinement, texture modification, and particle redistribution [33–35]. In this study, we explore, for the first time, SS-FSC's potential to fabricate composite wires with a controllable compositional gradient, exploiting its capability to achieve dense, well-formed composites with excellent particle dispersion through in-situ mixing. As a proof-of-concept, an SPS billet containing a step-change in SiC concentration was processed via SS-FSC to produce a graded composite wire. The resulting wire was extensively characterized for microstructure and mechanical properties to confirm the SiC concentration gradient and its effects on composite behaviour. Once validated, this concept can be readily multiplexed, providing an efficient high-throughput methodology for systematically exploring structure–property relationships across diverse novel (reinforced) alloy systems.

2. Experimental

The Mg alloy AZ91 used in this study was provided by non ferrum GmbH (Austria) as machinery chips (Fig. 1a, composition in Table 1), with average dimension of 5 mm × 1.5 mm × 1.5 mm (L × W × H). μm-sized 6H-SiC powder (325 mesh) supplied by Alfa Aesar (USA) had a measured maximum Feret diameter of 73 ± 17 μm, determined from SEM images of 100 particles (Fig. 1b).

Before SS-FSC, Samples were first processed by spark plasma sintering (SPS) using an FCT HPD25 machine (FCT Systeme GmbH, Germany). Before sintering, pure AZ91 chips and a manually stirred mixture of AZ91 chips with 1.1 vol% (2 wt%) SiC powder were loaded separately into an 80 mm diameter mould (15 mm thick), separated by graphite paper (configuration in Fig. 2b). After graphite paper removal, the mixture was pre-compacted under a 5 kg load. SPS was conducted at 500 °C under 35 MPa pressure and vacuum conditions for 10 min. post-sintering, the billet was mechanically ground to remove the oxide layer and milled flat for subsequent processing.

Stationary-shoulder friction stir channelling (SS-FSC) was performed at TWI, Cambridge, using an ESAB SuperStir™ machine equipped with TWI's stationary shoulder system [33]. These processing parameters were selected based on our previous experience extruding wires of other lightweight alloys [33–35]. A rotating MP159 nickel–cobalt alloy probe (6 mm diameter, 1200 RPM, 50 mm/min traverse speed) was used, producing wire through a 2 mm diameter hole in the stationary shoulder. Following SS-FSC (as shown in Fig. 2b), both the residual billet after SPS and the extruded wire (Fig. 3c) were characterised.

For metallographic characterization using optical microscopy (OM) and scanning electron microscopy (SEM) of the SPS billet, two samples with distinct compositions were extracted from each end of Path C (Fig. 3a–b). The extruded wire was sectioned into eight segments (approximately 2 cm each, labelled No. 1–No. 8; Fig. 3c) for analysis. All samples were prepared using standard metallographic polishing procedures, including diamond suspensions (1 μm, oil-based) followed by final polishing with an OPS–isopropanol mixture, for subsequent observation by SEM (Zeiss Sigma-300) and OM (OLYMPUS BX51). To reveal grain structures in samples subjected to SS-FSC processing, etched samples were prepared post-polishing using a solution composed of glacial acetic acid, deionised water, and ethanol in a volume ratio of 1:44:156.

For electron backscatter diffraction (EBSD) analysis (Bruker e-FlashHR for the wire, and Oxford Instruments C-Nano systems for the SPS billet), samples underwent additional broad Ar ion beam polishing using a Gatan PECS II system for 16 h following mechanical polishing. EBSD scans were conducted with step sizes of 1.5 μm for the billet and 0.5 μm for the wire, covering scanned areas of 823 × 672 μm^2 and 672 ×

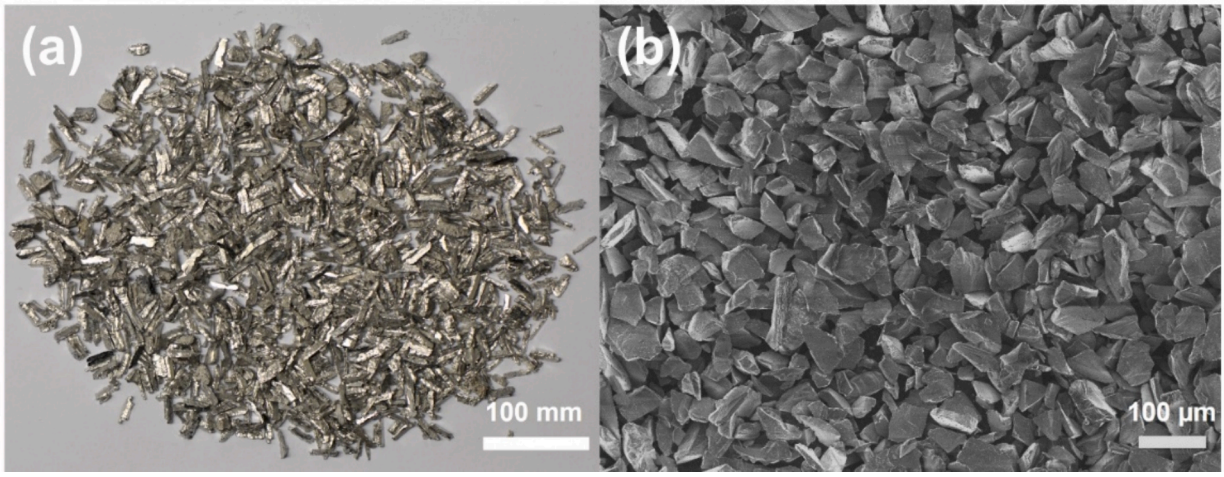

Fig. 1. (a) Optical image of AZ91 chips used in this study. (b) SEM image of the SiC microparticles used in this study.

Table 1
Elemental composition in weight fractions of AZ91 alloys used in this study.

Mg	*Al*	*Zn*	*Mn*	*Si*	*Cu*	*Ni*	*Fe*	*Be*	*others*
Balance	*8.500–9.500*	*0.450–0.900*	*0.170 – 0.400*	*0.000 – 0.080*	*0.000 – 0.025*	*0.000 – 0.001*	*0.000 – 0.004*	*0.000 – 0.001*	*0.000 – 0.010*

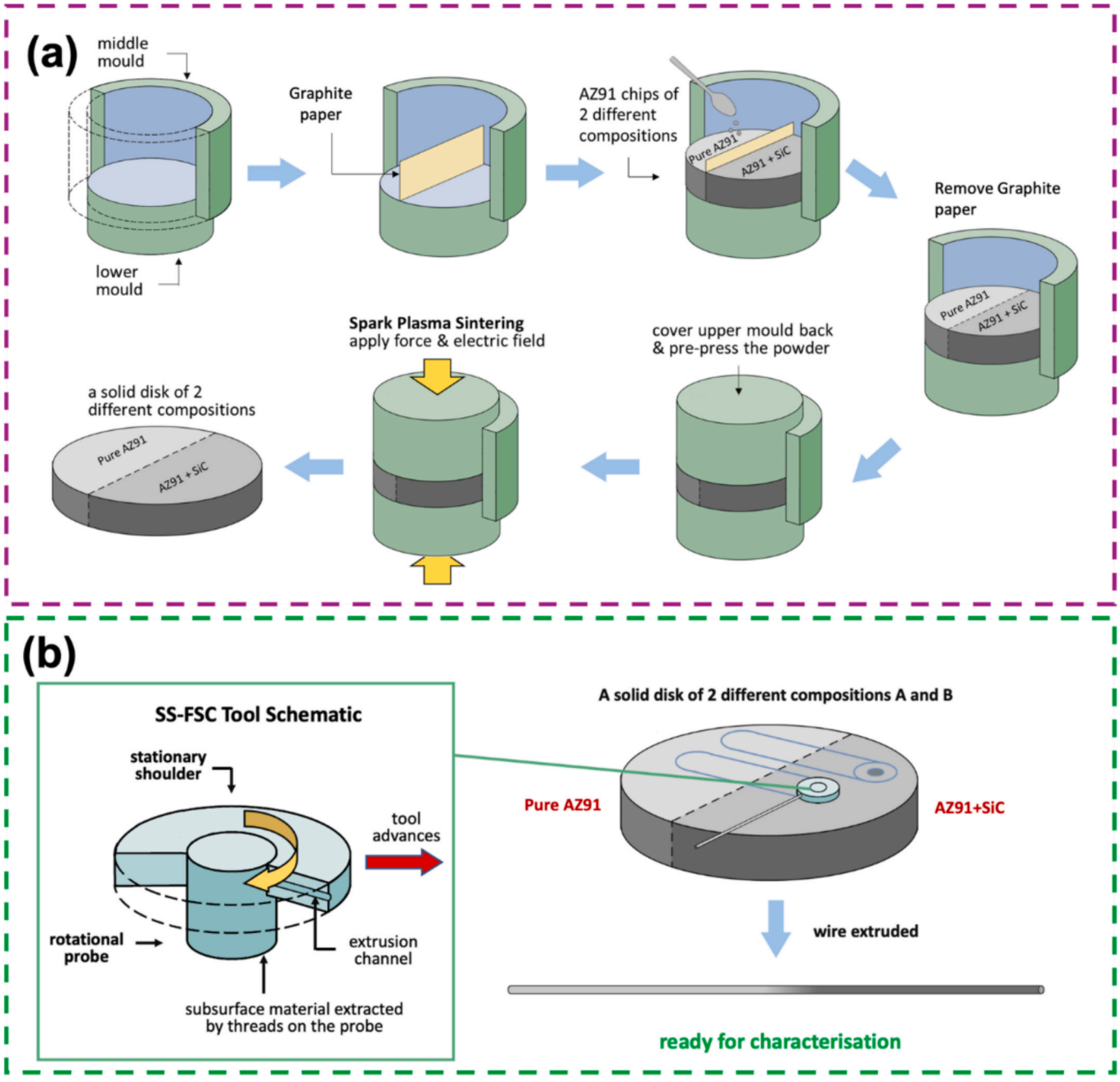

Fig. 2. Schematics of (a) the SPS process to fabricate a compositionally varying billet and (b) the SS-FSC process to convert the billet to a compositionally graded wire.

823 μm^2, respectively. SEM-EDX and EBSD analyses were conducted using Bruker's Esprit 2.1 and Oxford Instruments AztecCrystal software, identifying phases α-Mg [36] and 6H-SiC [37]. The EBSD data were then extracted and further analysed using MTEX 5.11.2 plugin in MATLAB 2023a (MathWorks, USA).

SiC concentration gradients were confirmed by segmenting SEM-BSE images into 1 mm sections and calculating the area fraction of SiC using ImageJ [38], detailed further in supplementary information (Fig. S1).

Hardness testing was conducted on an INDENTEC macrohardness tester with a 3 kg load and a 10 s dwell. Measurements were spaced 1 mm apart to avoid overlap of indentation marks (max diameter ~ 300 μm).

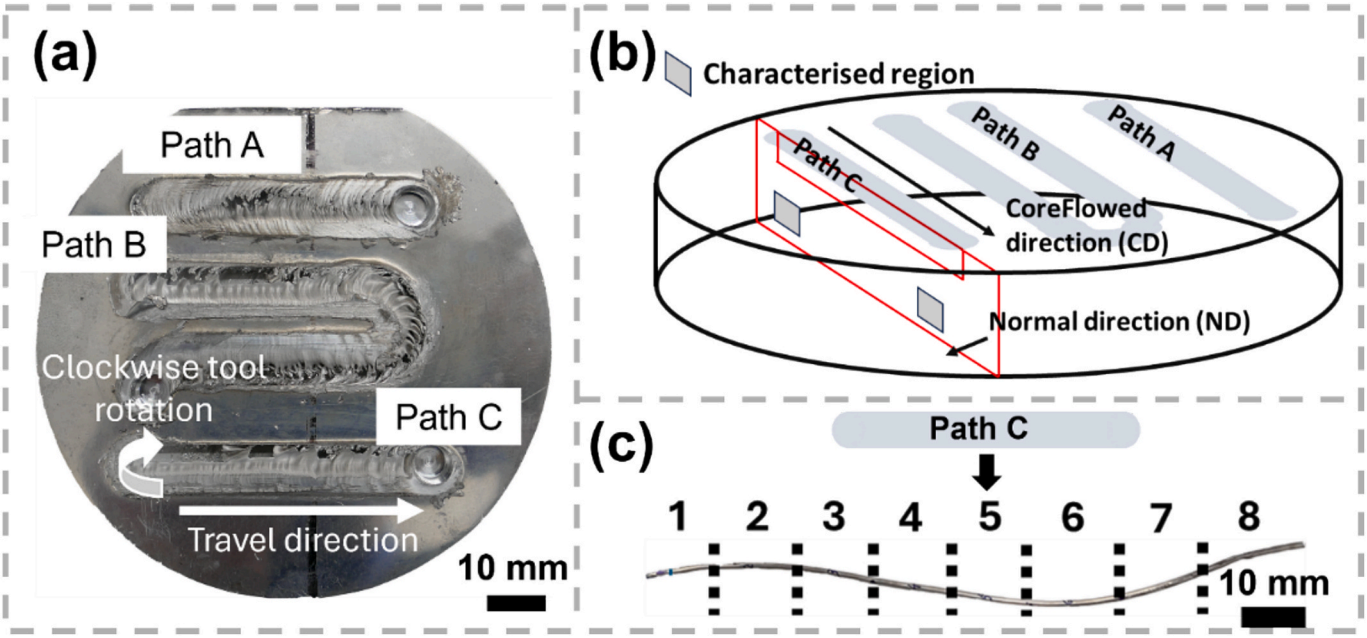

Fig. 3. (a) Optical image of the SPS billet after SS-FSC. (b) Regions of interest within SPS billet for microstructural characterisations. (c) Optical image of the wire after SS-FSC Path C. The wire was cut into eight near equal-length sections for characterisation. These sections were sequentially labelled as Sections 1–8, as illustrated in (c). The black dotted lines show the boundaries for each section.

3. Results and discussion

3.1. General microstructure of the billet after SPS

The SEM-BSE images of the two compositional sections within the SPS billet (Fig. 4a–b) highlight important phases present based on Z-contrast, including Al–Mn intermetallic compounds (Al–Mn IMCs), Mg_2Si, and micron-sized SiC particles, as indicated in the figure. No β-$Mg_{17}Al_{12}$ phase was identified in either section of the billet, likely due to the high processing temperature (500 °C) compared to the solution treatment temperature for AZ91 (413 °C) [39], the relatively long heating (6 min 30 s) and dwell time (10 min), and the rapid cooling rate during SPS. Additionally, no obvious porosity was identified in either section of the billet, suggesting that SPS effectively fabricated the dense billet required for SS-FSC. However, since most of the raw AZ91 chips did not melt during SPS processing, clusters of SiC particles located near the original chip boundaries were observed within the composite section.

The inverse pole figure (IPF) orientation maps of Mg in the two regions revealed the typical recrystallised grain structure obtained after SPS (Fig. 4c–d) [40]. Based on the colour coding in the orientation maps, a random crystallographic orientation was observed on both sides of the billet. Additionally, distinguishable boundaries resembling the outlines of the original AZ91 chips are also visible (labelled in Fig. 4c). This phenomenon is likely due to the heterogeneous nucleation of Mg grains on the native oxide layer of the chip surface [41], leading to a more random texture in the sintered billet. Finally, grain size measurements indicated slight refinement in the region with SiC addition (38.0 ± 1.9 μm) compared to the SiC-free region (44.3 ± 2.3 μm). We infer that the observed variation in Mg grain size is likely due to particle-stimulated nucleation (PSN) [42–46] induced by micron-sized SiC particles (Fig. 4d). Specifically, the significant strength difference between the Mg matrix (~100 MPa [41,47]) and SiC particles (up to 8.4 GPa [48]) results in a misorientation gradient accumulating within the Mg matrix surrounding the SiC particles during SPS. This gradient provides the driving force for transforming sub-grain boundaries within the Mg matrix into high-angle grain boundaries.

3.2. General microstructure and phase analysis of the extruded wire after SS-FSC

The dimensions of the extruded wire after Path C (path length: 50 mm) were 160 mm in length and an average diameter of 1.6 mm (Fig. 3). Analysis of optical microscopy (OM) images of the entire wire, in both longitudinal (Fig. 5) and radial (Fig. S2) cross-sections, revealed a significant improvement in SiC distribution and dispersion compared to the billet after SPS, with no obvious particle clustering. No waste material was generated during the wire extrusion process, demonstrating the high efficiency of the CoreFlow technique. Additionally, most wire sections exhibited good structural integrity, with no obvious porosity observed in the wire's central cross-section. However, some surface cracks were observed in certain sections of the extruded wire (e.g., Sections No. 2 and No. 8), likely due to fluctuations in the extrusion rate. These fluctuations could be attributed to various factors, such as inconsistencies in the parent material, variations in process temperature, and adhesion issues during extrusion [49,50].

The phase distribution within the extruded wire was further analysed using high-magnification OM and BSE imaging in Section No. 5 (Fig. 6c, e and Fig. 6d,f). SEM-EDX point analysis revealed a finer and more uniform distribution of secondary phases, such as Al–Mn intermetallic compounds and Mg_2Si, within the extruded wire compared to the billet after SPS. These results are similar to our previous observations of extruded AZ31 wires from SS-FSC, where the redistribution of secondary particles was observed [33]. Additionally, regions approximately 10 μm thick exhibiting features such as cracks or flow lines were frequently observed surrounding individual SiC particles (Fig. 6f). Given the high strength and modulus of the SiC particles, these regions are attributed to stress concentration during the extrusion process. The formation of such regions may adversely affect the mechanical performance of the extruded wire by causing stress concentration and promoting premature crack initiation during loading. However, the size of these stress-concentrated regions is expected to decrease monotonically with the use of smaller reinforcement particles in future studies [42].

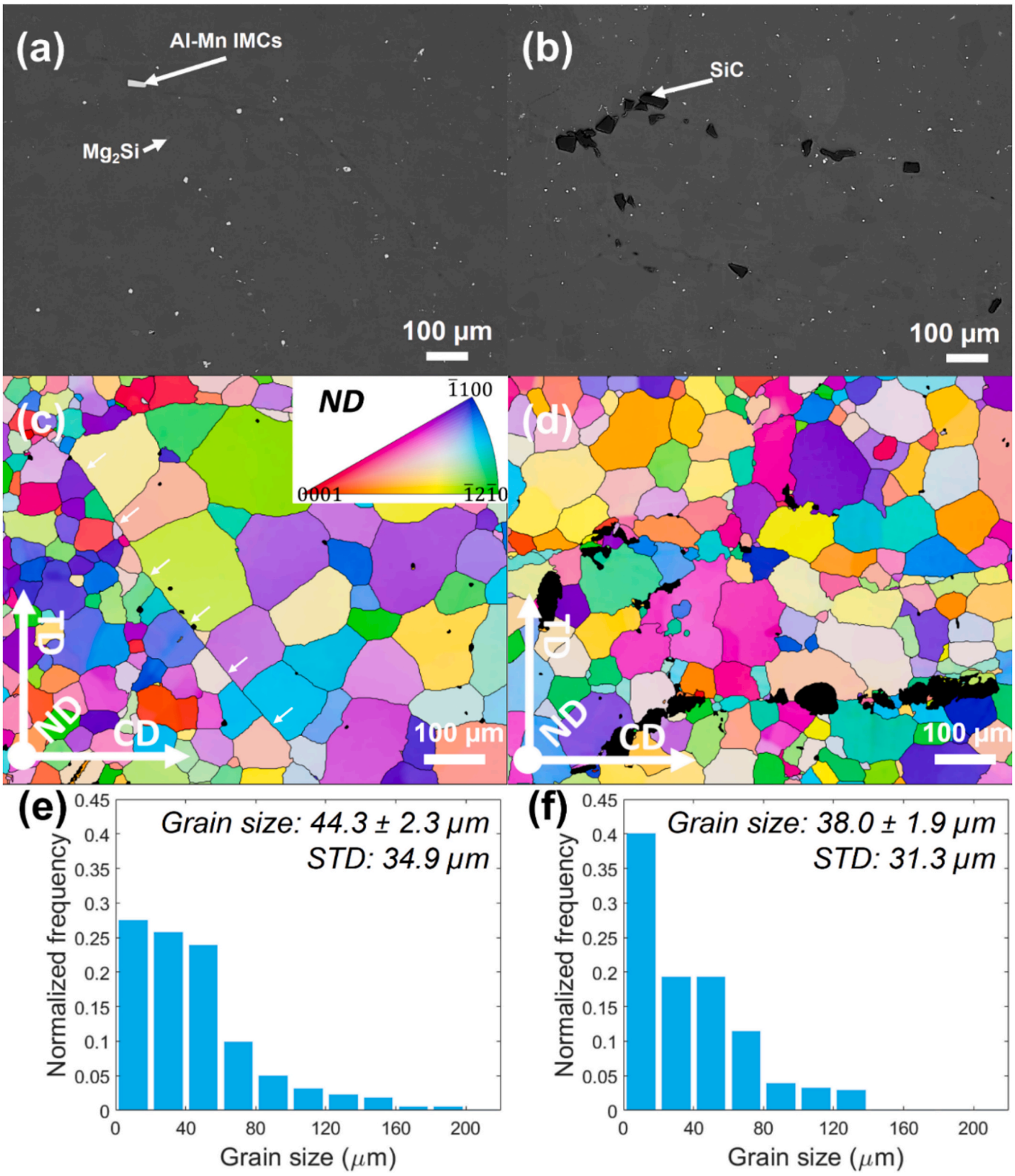

Fig. 4. SEM-BSE images of (a) pure AZ91 and (b) AZ91-SiC sides of the SPSed billet. IPF orientation map viewing from the normal direction (ND) (as indicated in Fig. 3b) in the (c) pure AZ91 and (d) AZ91-SiC sides of the billet. CD and TD in the label stand for CoreFlow® direction and transverse direction, respectively. Grain size distribution for the (e) pure AZ91 and (f) AZ91-SiC sides of the billet, determined from the EBSD data.

3.3. *Graded structure in the extruded wire*

By comparing the distribution of SiC particles (which appear as dark contrast regions) across all eight longitudinal sections of the extruded wire (Fig. 5), a concentration gradient was identified between Sections No. 5 and No. 6. The calculated SiC area fraction as a function of position (Fig. 7) — derived from SEM-BSE images of Sections 5 and 6 (Fig. 6b and Fig. S3; see Supplementary Information for details) and trend lines in

Fig. 5. Stitched OM images of all the 8 cross-sections in the extruded wire, with Section No.1 at the top to Section No.8 at the bottom.

Fig. 7 — reveal that SiC content becomes negligible beyond 33 mm from the left edge of Section No. 5, indicating a transition to pure alloy. In contrast, within the 0–17 mm region, a SiC-rich zone with an average volume fraction of approximately 1.5 vol% was observed. The observed scattering in volume fraction is likely results from uneven pre-mixing of SiC particles with AZ91 chips before SPS.

Given the 6-mm diameter of the rotating probe used in this study (see Supplementary Video 1) and the total length of wire produced, the effective extrusion rate is estimated at roughly 3 mm of wire per mm of probe travel. This conversion rate implies that a sharp compositional boundary in the original billet would be transferred into a graded region approximately 18 mm long during extrusion. This estimate closely matches the experimentally observed compositional gradient of approximately 16 ± 2-mm-long compositional gradient (Fig. 7), although it is somewhat obscured by the coarse size of the SiC particles. Composition transitions over this length scale offer the opportunity to measure a range of properties along the wire length, allowing rapid assessment of material performance across multiple compositions originating from each step-change in the source billet.

3.4. Microstructure and mechanical performance across the SiC gradient

To examine the influence of SiC concentration on microstructural evolution, EBSD mapping was conducted on Section No.5 and No.6 (Fig. 8). SEM-BSE imaging confirmed that the SiC concentrations in the EBSD-scanned regions were 1.25 vol% and 0.00 vol%, respectively. The IPF maps revealed that the microstructure of the wire after SS-FSC exhibited fully recrystallized grains with a duplex grain-size distribution and a strong basal texture aligned along the extrusion direction. This duplex grain-size distribution is consistent with previous observations in AZ31 wires processed by SS-FSC [33].

The average grain sizes of the pure AZ91 wire section and the composite wire section were measured to be 7.4 ± 0.5 μm (Fig. 8a) and 5.1 ± 0.5 μm (Fig. 8b), respectively. Compared to the corresponding sections of the billet after SPS, the average grain size exhibited a significant reduction of approximately 85% in both wire sections. This observation is consistent with our previous study on AZ31, confirming the grain-refinement capability of the SS-FSC process [33]. When comparing the two wire sections, a small but significant decrease in grain size was observed upon the addition of SiC. This observation is further illustrated in Fig. 9, where fine grains were observed surrounding the SiC particles. Similar to the modestly refined grains observed in the parent billet (Fig. 4d), this phenomenon is attributed to particle-stimulated nucleation (PSN) associated with misorientation gradients around the SiC particles (Fig. 9) [42]. This observation aligns with previous studies [43–46], where PSN was similarly induced by adding hard TiC nanoparticles during friction stir welding of Mg and Al alloys.

Unfortunately, the anticipated gradient in grain structure across the

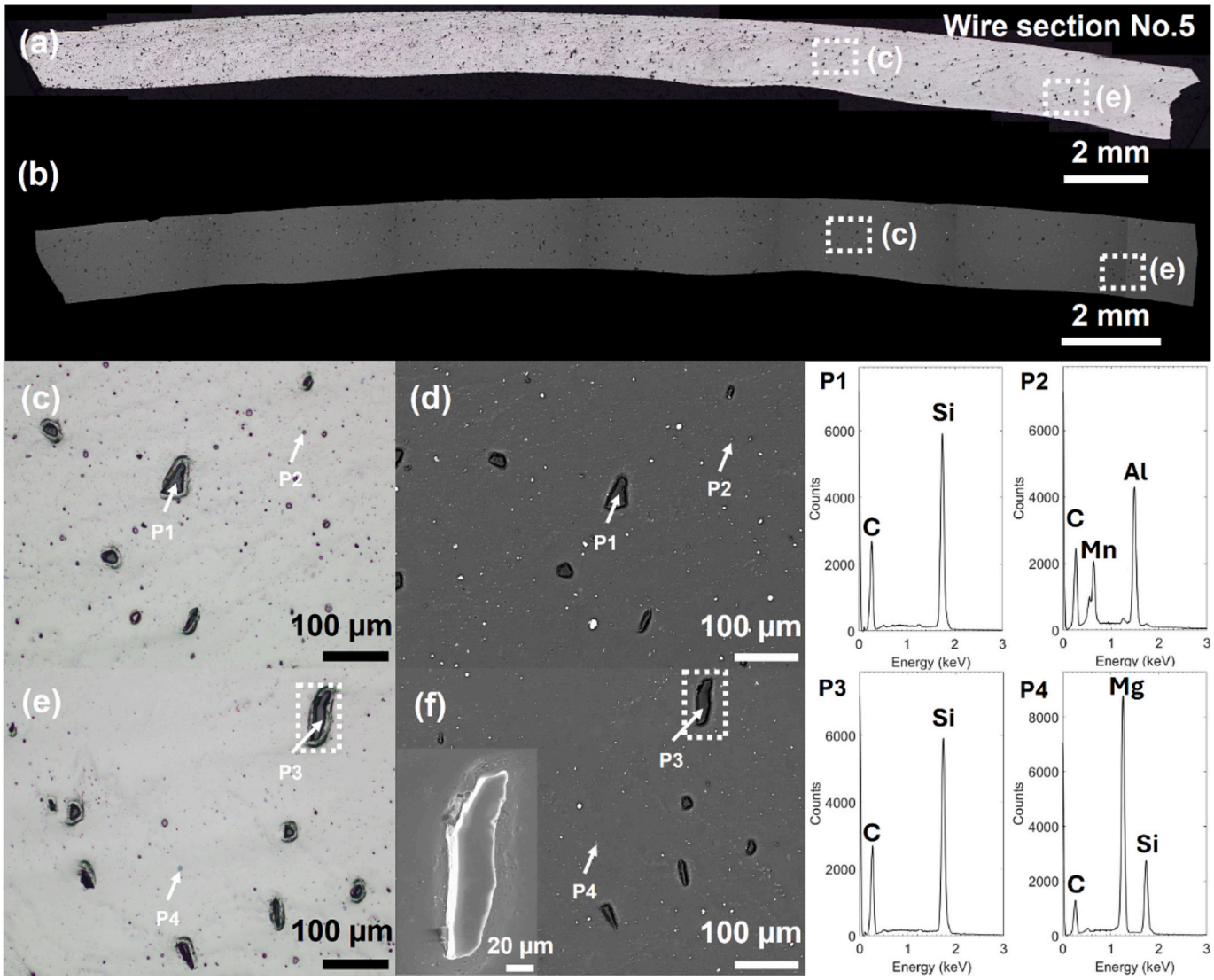

Fig. 6. (a) Stitched OM image & (b) SEM-BSE image of the whole cross-section of wire section No. 5. (c) & (e) Zoomed-in OM images of the regions labelled in (a). (d) & (f) SEM-BSE images of region in (c) and (e). Within the zoomed in OM and SEM-BSE images, the locations of SEM-EDX point analyses P1-P4 are labelled with white arrows and the spectra collected are shown on the right-hand side. The inset of (f) is the SEM-secondary electron image of the SiC particle indicated by the white box in (f).

graded SiC region was not observed (Fig. S4), due to the presence of fine recrystallised grains formed during the welding of the wire as it passed through the helical thread of the rotating SS-FSC probe (Fig. S4) [33]. Future work will focus on modifying the probe design to minimise or eliminate the formation of such inhomogeneous grain structure by optimising probe design, Nevertheless, the microstructure investigation showed the ability of forming graded grain structure with graded SiC across the wire.

To investigate the effect of SiC concentration on the mechanical performance of the wire after SS-FSC, hardness measurements were performed across the region exhibiting a SiC concentration gradient, as shown in Fig. 7. The resulting hardness values (Fig. 10) ranged from 62 HV3 to 72 HV3. These values are consistent with the hardness ranges reported in previous studies for AZ91 alloys [25,31,51–55] and their SiC composite [32,56–59] billets after friction stir processing, supporting the validity of the present measurements.

The observed fluctuations in the hardness measurement are attributed to the relatively large interparticle spacing of SiC compared to the size of the hardness indenter (Fig. S5). Despite this variability, a clear correlation between SiC concentration (Fig. 7) and hardness was observed (Fig. 10). Specifically, the average hardness in the SiC-rich region (Section No. 5) was 68.9 ± 2.7 HV3, which is 3.1 HV3 higher than that in the SiC-free region (65.8 ± 1.2 HV3). Moreover, a 6 mm-long hardness gradient (between 20 and 26 mm) was observed, which is approximately half of the composition gradient (Fig. 7) due to the localised nature of the hardness measurement (Fig. S5). It is anticipated that future studies employing finer reinforcements and minimising grain structure inhomogeneity across the wire, particularly that associated with the weld lines, will allow a clearer correlation between composition and mechanical performance to be established.

3.5. *Influence from the SS-FSC stir probe*

During the microstructural analysis, particles exhibiting bright contrast were frequently observed around the SiC particles, as highlighted by the white arrow in Fig. 11. The EDX point analysis spectrum collected from one of these bright particles, labelled as P1 (Fig. 11b), revealed characteristic peaks corresponding to Cr, Co, and Mo, matching the elemental composition of the stir probe made from MP159 alloy [60]. The area fraction of bright contrast particles (including Al–Mn

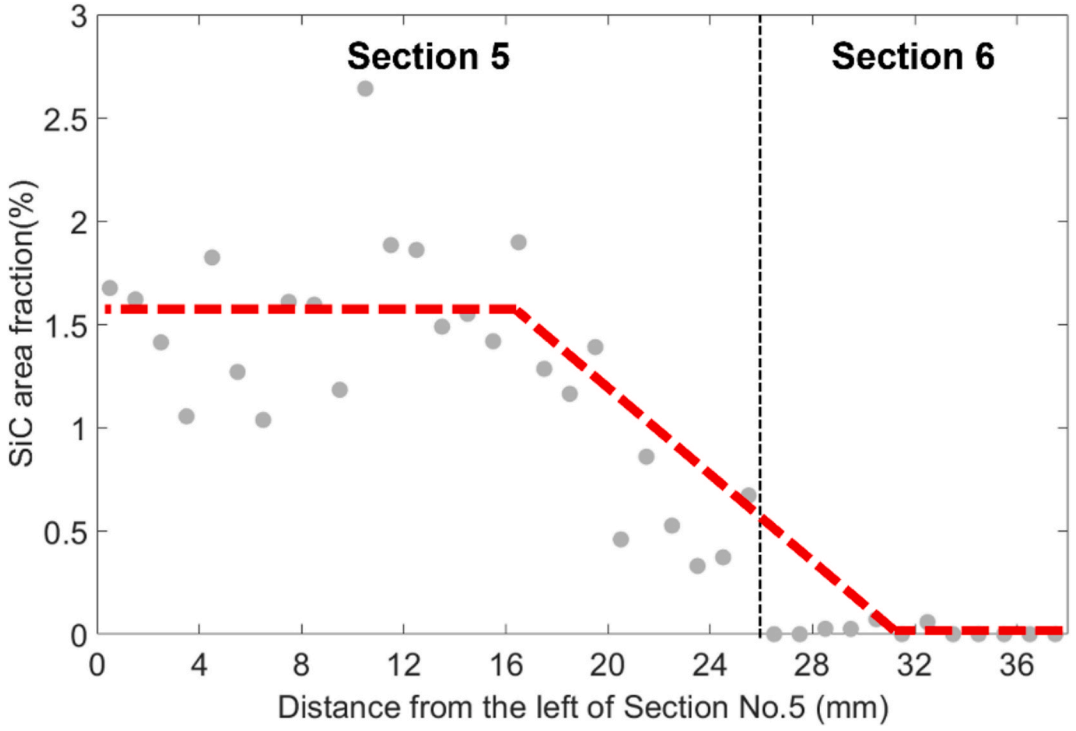

Fig. 7. Plot of SiC area fraction along sections No. 5 and No. 6, deduced by image analysis. The red dotted lines offer a visual guide to the average SiC area fraction and a trend in SiC area fraction variation in the alloy, transition and composite sections of the wire.

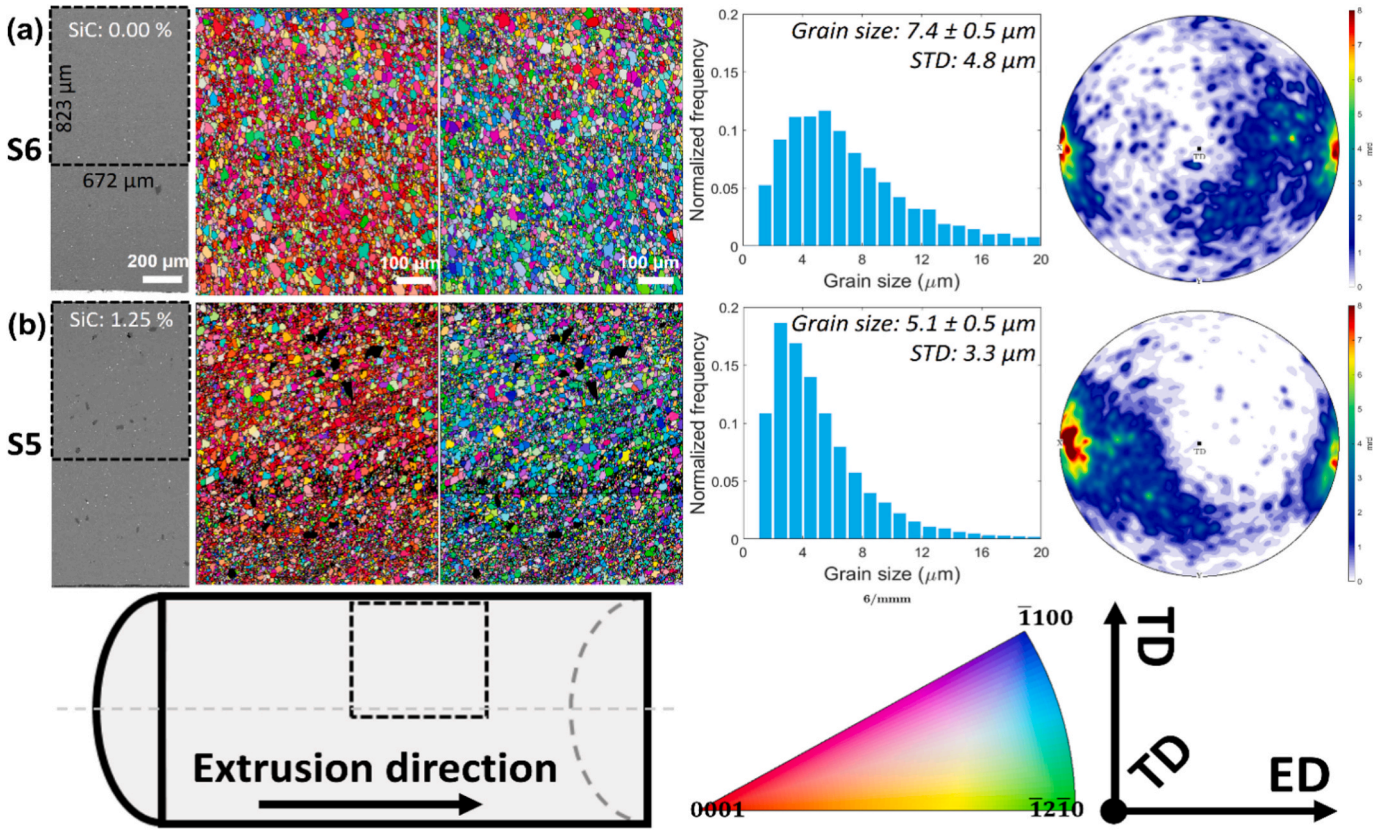

Fig. 8. SEM-EBSD analysis of wire Sections No. 6 (S6) and 5 (S5) after extrusion (a–b). For each wire section, an SEM-BSE image, IPF-ED and IPF-TD maps, grain size distribution, and pole figure of the EBSD-scanned region (marked by a black dotted line in the SEM-BSE image) and the wire cross-section sketch are provided. The IPF maps were cropped and stitched from two EBSD scans to create a scanned region of 672 µm × 823 µm. All the SEM-BSE images and IPF orientation maps in this figure were captured at the same magnification.

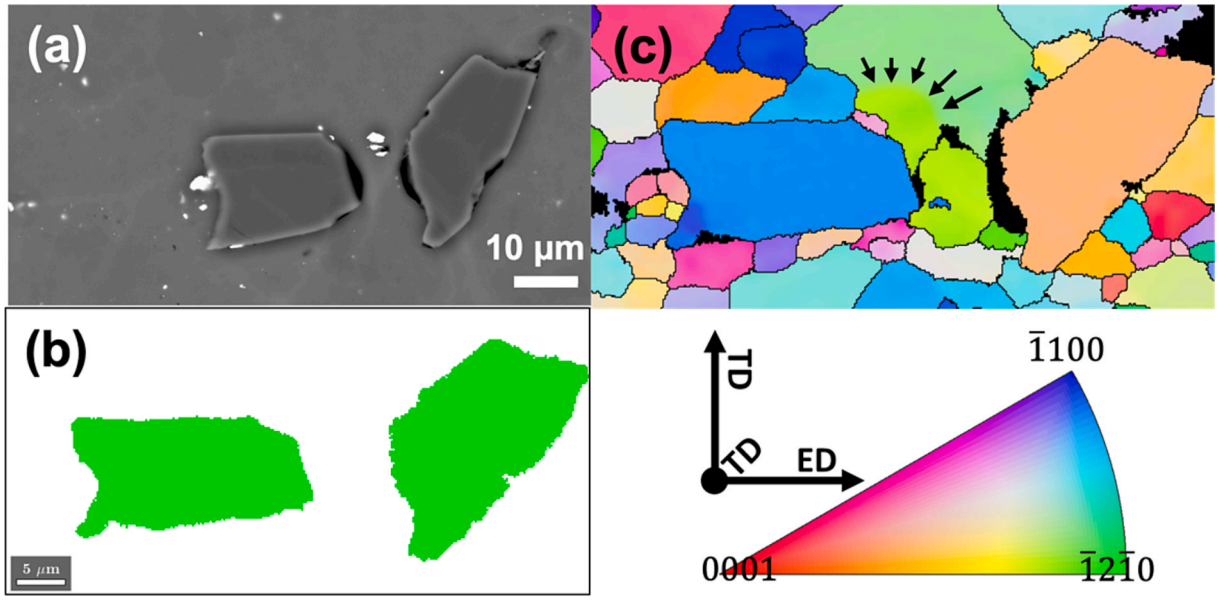

Fig. 9. EBSD scanning results around two micro-sized SiC particles found within wire Section No.5 (Fig. 8b). (a) SEM-BSE image of the EBSD scanned region. (b) Phase map from the EBSD results, with α-Mg color-coded in white and 6H-SiC in green. (c) IPF-TD map of α-Mg and 6H-SiC in the scanned region. The sub-grain boundary caused by misorientation around SiC is marked by black arrows.

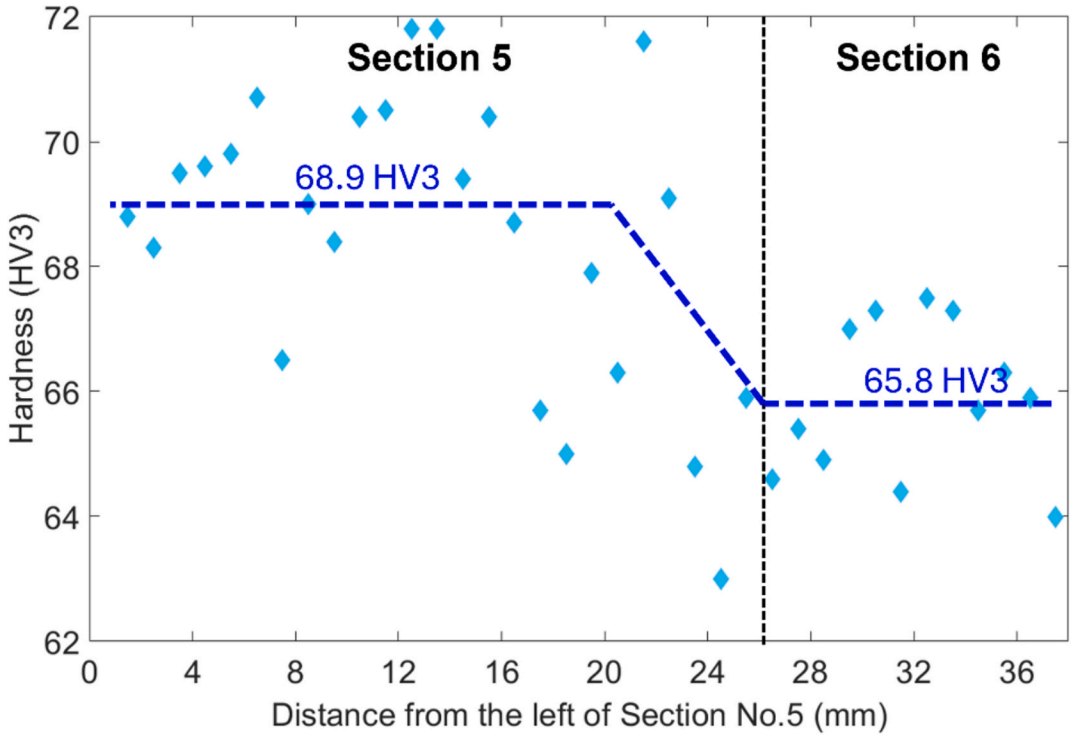

Fig. 10. Hardness measurements in wire Sections No.5 and No.6. The measurements were performed on each section separated by 1 mm. The blue dotted lines offer a visual guide to the average hardness and the trend in hardness variation in the alloy, transition and composite sections of the wire.

intermetallic compounds and MP159 alloy debris) increased approximately fourfold when comparing wire sections containing high SiC loading (Fig. 11c) to sections with negligible SiC content (Fig. 11d). Thus, these particles are proposed to be debris resulting from abrasion between SiC particles and the stir probe during SS-FSC. Cleavage features and cracks observed within individual SiC particles (left-hand side of Fig. 11a) further support this assumption. The presence of this hard debris may also contribute to fluctuations in hardness measurements (Fig. 10) and unintended grain refinement of the alloy matrix through mechanisms such as particle-stimulated nucleation (PSN). In future studies, probe erosion might be mitigated by using smaller filler particles [61]. If necessary, the material selection for the SS-FSC stir probe could be optimised or modified, for instance, by applying hard coatings to reduce erosion.

4. Conclusions

This study presents a novel approach for producing AZ91 matrix

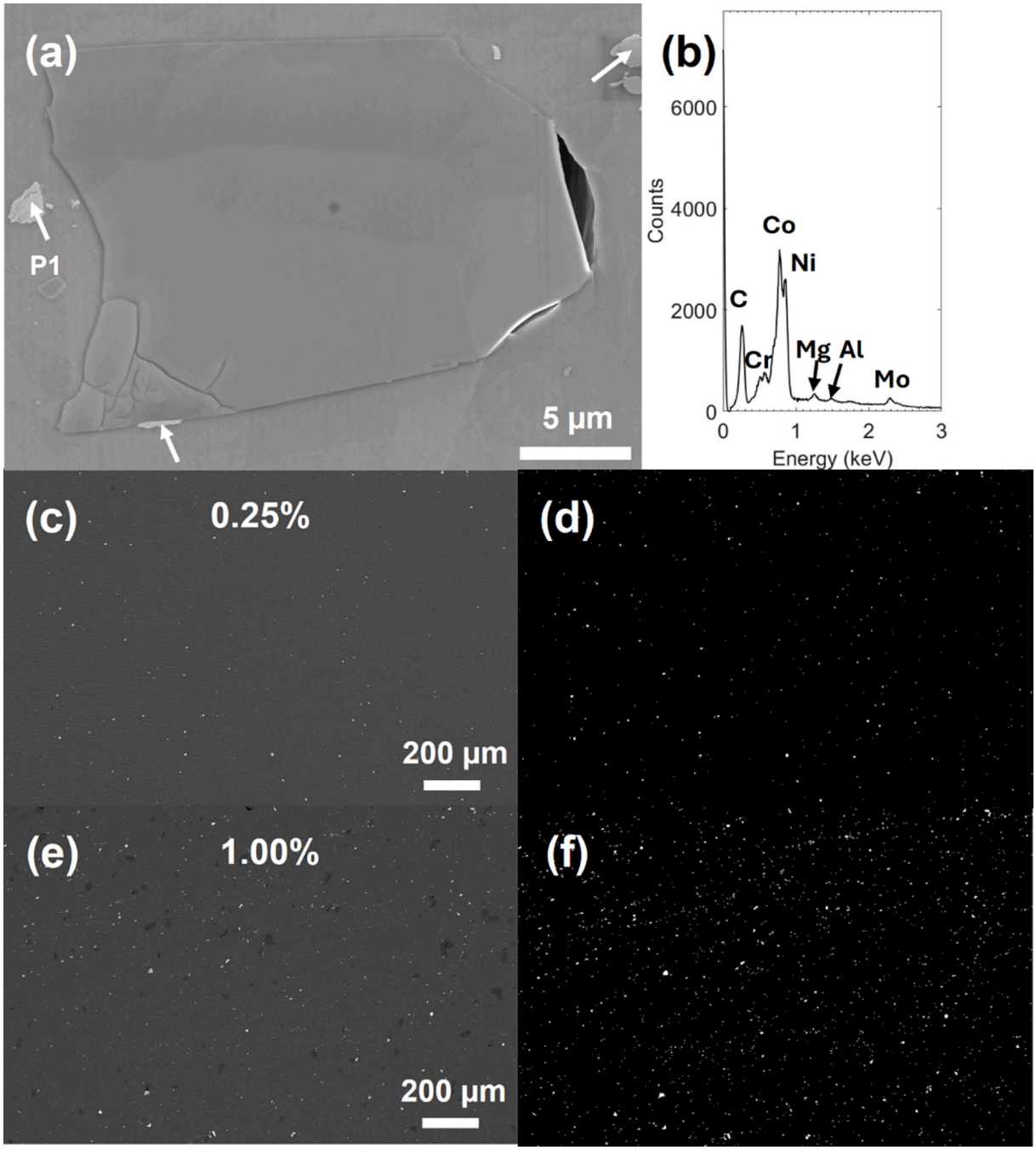

Fig. 11. (a) SEM image of a SiC particle in Section No.5 after ion milling. Debris caused by stir probe erosion was identified near the particle, indicated with the white arrow. (b) EDX spectrum collected from point analysis at location P1. (c-d) SEM-BSE image and the image segmentation result showing the distribution of these debris in a wire section without SiC loading. (e-f) SEM-BSE image and the image segmentation result showing the distribution of these debris in a wire section with SiC loading. The area fraction of the bright contrast particles within the images was also calculated and is labelled on the SEM images.

composite wires with a longitudinal SiC concentration gradient, achieved for the first time through a combination of spark plasma sintering (SPS) and stationary-shoulder friction stir channelling (SS-FSC).

Microstructural analysis revealed a 16-mm-long SiC concentration gradient (ranging from approximately 1.5 vol% to 0 vol%), originating from a single abrupt compositional interface (approximately 1.1 vol% to 0 vol%) within the SPS-fabricated feedstock. This compositional gradient also shows a potential in forming a graded grain structure, with refined grains observed in regions containing 1.25 vol% SiC (5.1 ± 0.5 μm), compared to larger grains in the SiC-free region (7.4 ± 0.5 μm), attributed to particle-stimulated nucleation. The mechanical study via hardness measurements confirmed a positive correlation between the graded SiC and mechanical performance. The average hardness increased from 65.8 ± 1.2 HV3 in the pure AZ91 region to 68.9 ± 2.7 HV3 in the high-SiC concentration region.

While the quality of the wires produced using this method is good, surface finish and dimensional consistency could be improved by optimising the extrusion parameters more specifically for Mg-based alloys. The homogeneity of the wires could be improved by mixing reinforcement particles with finer metal powders or by enhancing pre-mixing of the alloy chips and SiC particles prior to SPS, for example, using ball milling [62] or wet pre-mixing [63,64]. Smaller filler particles will also create more homogeneous property gradients and limit erosion of the SS-FSC probe. Consistent, locally homogeneous wires will be well suited

to the development of range of other local property evaluations, for subsequent correlation with the local microstructure.

In summary, this study outlines a proof-of-concept for a fresh approach to the exploration of new (reinforced) alloy compositions. It confirms the hypothesis that SS-FSC can serve as an effective method for producing longitudinally graded alloy/MMC wires well-suited to structure–property characterisation. The linear configuration is particularly appealing due to its compatibility with various continuous evaluation techniques. The number of compositions in the SPS billet can be readily increased to encode numerous compositions within the resulting wires, enabling the creation of a novel high-throughput approach for rapid composite prototyping. Sets of encoded wires could be subjected to different thermal treatments to make further connections between composition, microstructure, and properties. In future work, this method could be extended to other alloy systems (e.g., RE-containing Mg alloys [65], Al alloys [66] and high-entropy alloys [15]) or different types of reinforcements (e.g. CNT [64], nano-SiC [67]) to accelerate the prototyping and development of novel alloys and composites.

CRediT authorship contribution statement

Zhuocheng Xu: Writing – original draft, Validation, Methodology, Investigation, Formal analysis, Data curation. **Xingjian Zhao:** Methodology, Investigation, Formal analysis. **Oliver Watts:** Methodology, Investigation, Data curation. **W. Mark Rainforth:** Writing – review & editing, Supervision, Investigation. **Milo S.P. Shaffer:** Writing – review & editing, Validation, Supervision, Investigation, Conceptualization. **Sam Holdsworth:** Writing – review & editing, Validation, Resources, Investigation, Data curation. **Dikai Guan:** Writing – review & editing, Supervision, Resources, Investigation, Formal analysis. **Qianqian Li:** Writing – review & editing, Validation, Supervision, Resources, Methodology, Investigation, Conceptualization.

Declaration of competing interest

The authors declare that they have no known competing financial interests or personal relationships that could have appeared to influence the work reported in this paper.

Acknowledgement

The authors wish to acknowledge the use of characterisation facilities within the Harvey Flower Electron Microscopy Suite, Imperial College London. The authors also wish to acknowledge the technical support and great help from Mr Peter Schäffler and Mr Matthew Herbert at Non Ferrum GmbH regarding Mg AZ91 chips machining. The authors also wish to acknowledge the support with trials conducted at TWI Ltd., United Kingdom, provided by Nathan Horrex. DG acknowledges the support from the UKRI via the Future Leaders Fellowship (grant No. MR/T019123/2).

Appendix A. Supplementary data

Supplementary data to this article can be found online at https://doi.org/10.1016/j.matdes.2025.114016.

Data availability

Data will be made available on request.

References

[1] H. Dieringa, Properties of magnesium alloys reinforced with nanoparticles and carbon nanotubes: A review, J. Mater. Sci. 46 (2011) 289–306, https://doi.org/10.1007/s10853-010-5010-6.
[2] H. Guan, H. Xiao, S. Ouyang, A. Tang, X. Chen, J. Tan, B. Feng, J. She, K. Zheng, F. Pan, A review of the design, processes, and properties of Mg-based composites, Nanotechnol. Rev. 11 (2022) 712–730, https://doi.org/10.1515/ntrev-2022-0043.
[3] W. Zhang, J. Xu, Advanced lightweight materials for Automobiles: A review, Mater. Des. 221 (2022) 110994, https://doi.org/10.1016/j.matdes.2022.110994.
[4] H.Z. Ye, X.Y. Liu, Review of recent studies in magnesium matrix composites, J. Mater. Sci. 39 (2004) 6153–6171, https://doi.org/10.1023/B:JMSC.0000043583.47148.31.
[5] R. Casati, M. Vedani, Metal matrix composites reinforced by nano-particles—A review, Metals (Basel). 4 (2014) 65–83, https://doi.org/10.3390/met4010065.
[6] A. Mortensen, J. Llorca, Metal matrix composites, Annu. Rev. Mater. Res. 40 (2010) 243–270, https://doi.org/10.1146/annurev-matsci-070909-104511.
[7] M. Ghorbani, M. Boley, P.N.H. Nakashima, N. Birbilis, A machine learning approach for accelerated design of magnesium alloys. Part B: regression and property prediction, J. Magnes. Alloy. 11 (2023) 4197–4205, https://doi.org/10.1016/j.jma.2023.09.010.
[8] J.J. de Pablo, N.E. Jackson, M.A. Webb, L.-Q. Chen, J.E. Moore, D. Morgan, R. Jacobs, T. Pollock, D.G. Schlom, E.S. Toberer, J. Analytis, I. Dabo, D. M. DeLongchamp, G.A. Fiete, G.M. Grason, G. Hautier, Y. Mo, K. Rajan, E.J. Reed, E. Rodriguez, V. Stevanovic, J. Suntivich, K. Thornton, J.-C. Zhao, New frontiers for the materials genome initiative, Npj Comput. Mater. 5 (2019) 41, https://doi.org/10.1038/s41524-019-0173-4.
[9] V. Chaudhary, R. Chaudhary, R. Banerjee, R.V. Ramanujan, Accelerated and conventional development of magnetic high entropy alloys, Mater. Today 49 (2021) 231–252, https://doi.org/10.1016/j.mattod.2021.03.018.
[10] D. Miracle, B. Majumdar, K. Wertz, S. Gorsse, New strategies and tests to accelerate discovery and development of multi-principal element structural alloys, Scr. Mater. 127 (2017) 195–200, https://doi.org/10.1016/j.scriptamat.2016.08.001.
[11] S. Shukla, T. Wang, M. Frank, P. Agrawal, S. Sinha, R.A. Mirshams, R.S. Mishra, Friction stir gradient alloying: A novel solid-state high throughput screening technique for high entropy alloys, Mater. Today Commun. 23 (2020) 100869, https://doi.org/10.1016/j.mtcomm.2019.100869.
[12] B.L. Bresnahan, D.L. Poerschke, High-throughput multi-principal element alloy exploration using a novel composition gradient sintering technique, Metals (Basel). 14 (2024) 558, https://doi.org/10.3390/met14050558.
[13] T. Borkar, B. Gwalani, D. Choudhuri, C.V. Mikler, C.J. Yannetta, X. Chen, R. V. Ramanujan, M.J. Styles, M.A. Gibson, R. Banerjee, A combinatorial assessment of AlxCrCuFeNi2 (0 < x < 1.5) complex concentrated alloys: microstructure, microhardness, and magnetic properties, Acta Mater. 116 (2016) 63–76, https://doi.org/10.1016/j.actamat.2016.06.025.
[14] B. Gwalani, S. Gangireddy, S. Shukla, C.J. Yannetta, S.G. Valentin, R.S. Mishra, R. Banerjee, Compositionally graded high entropy alloy with a strong front and ductile back, Mater. Today Commun. 20 (2019) 100602, https://doi.org/10.1016/j.mtcomm.2019.100602.
[15] M.A. Melia, S.R. Whetten, R. Puckett, M. Jones, M.J. Heiden, N. Argibay, A. B. Kustas, High-throughput additive manufacturing and characterization of refractory high entropy alloys, Appl. Mater. Today 19 (2020) 100560, https://doi.org/10.1016/j.apmt.2020.100560.
[16] A. Janghorban, J. Pfetzing-Micklich, J. Frenzel, A. Ludwig, Investigation of the Thin- <scp>F</scp> ilm phase diagram of the Cr– <scp>N</scp> i– <scp>R</scp> e system by High- <scp>T</scp> hroughput experimentation, Adv. Eng. Mater. 16 (2014) 588–593, https://doi.org/10.1002/adem.201300430.
[17] A. Ludwig, R. Zarnetta, S. Hamann, A. Savan, S. Thienhaus, Development of multifunctional thin films using high-throughput experimentation methods, Int. J. Mater. Res. 99 (2008) 1144–1149, https://doi.org/10.3139/146.101746.
[18] A. Kauffmann, M. Stüber, H. Leiste, S. Ulrich, S. Schlabach, D.V. Szabó, S. Seils, B. Gorr, H. Chen, H.J. Seifert, M. Heilmaier, Combinatorial exploration of the high entropy alloy system Co-Cr-Fe-Mn-Ni, Surf. Coatings Technol. 325 (2017) 174–180, https://doi.org/10.1016/j.surfcoat.2017.06.041.
[19] B. Saleh, J. Jiang, R. Fathi, T. Al-hababi, Q. Xu, L. Wang, D. Song, A. Ma, 30 Years of functionally graded materials: an overview of manufacturing methods, applications and future challenges, Compos. Part B Eng. 201 (2020) 108376, https://doi.org/10.1016/j.compositesb.2020.108376.
[20] B. Saleh, A. Ma, R. Fathi, N. Radhika, B. Ji, J. Jiang, Wear characteristics of functionally graded composites synthesized from magnesium chips waste, Tribol. Int. 174 (2022) 107692, https://doi.org/10.1016/j.triboint.2022.107692.
[21] G. Jamali, S. Nourouzi, R. Jamaati, Manufacturing of gradient Al/SiC composite wire by friction stir back extrusion, CIRP J. Manuf. Sci. Technol. 35 (2021) 735–743, https://doi.org/10.1016/j.cirpj.2021.09.004.
[22] M.J. Oza, K.G. Schell, E.C. Bucharsky, T. Laha, S. Roy, Developing a hybrid Al–SiC-graphite functionally graded composite material for optimum composition and mechanical properties, Mater. Sci. Eng. A 805 (2021) 140625, https://doi.org/10.1016/j.msea.2020.140625.
[23] H. Springer, D. Raabe, Rapid alloy prototyping: compositional and thermo-mechanical high throughput bulk combinatorial design of structural materials based on the example of 30Mn-1.2C-xAl triplex steels, Acta Mater. 60 (2012) 4950–4959, https://doi.org/10.1016/j.actamat.2012.05.017.
[24] T. Wang, S. Shukla, M. Komarasamy, K. Liu, R.S. Mishra, Towards heterogeneous AlxCoCrFeNi high entropy alloy via friction stir processing, Mater. Lett. 236 (2019) 472–475, https://doi.org/10.1016/j.matlet.2018.10.161.
[25] Q.S. Zhang, L. Xiao, K. Chen, M. Wang, X.M. Hua, L.T. Zhang, A.D. Shan, H. Wang, Friction stir high-throughput synthesis to evaluate the effect of Al on AZ Mg alloys, Mater. Lett. 284 (2021) 128924, https://doi.org/10.1016/j.matlet.2020.128924.
[26] R. Ivanov, A. Deschamps, F. De Geuser, High throughput evaluation of the effect of Mg concentration on natural ageing of Al-Cu-Li-(Mg) alloys, Scr. Mater. 150 (2018) 156–159, https://doi.org/10.1016/j.scriptamat.2018.03.024.

[27] B. Saleh, R. Fathi, N. Radhika, Z. Yu, S. Liu, L. Zhang, Effect of yttrium oxide on microstructure and mechanical properties of functionally graded magnesium matrix composites, J. Alloys Compd. 981 (2024) 173723, https://doi.org/10.1016/j.jallcom.2024.173723.
[28] C. Haase, F. Tang, M.B. Wilms, A. Weisheit, B. Hallstedt, Combining thermodynamic modeling and 3D printing of elemental powder blends for high-throughput investigation of high-entropy alloys – towards rapid alloy screening and design, Mater. Sci. Eng. A 688 (2017) 180–189, https://doi.org/10.1016/j.msea.2017.01.099.
[29] M. Hans, P. Keuter, A. Saksena, J.A. Sälker, M. Momma, H. Springer, J. Nowak, D. Zander, D. Primetzhofer, J.M. Schneider, Opportunities of combinatorial thin film materials design for the sustainable development of magnesium-based alloys, Sci. Rep. 11 (2021) 1–9, https://doi.org/10.1038/s41598-021-97036-6.
[30] M. Barati, M. Abbasi, M. Abedini, The effects of friction stir processing and friction stir vibration processing on mechanical, wear and corrosion characteristics of Al6061/SiO2 surface composite, J. Manuf. Process. 45 (2019) 491–497, https://doi.org/10.1016/j.jmapro.2019.07.034.
[31] B. Bagheri, A. Abdollahzadeh, M. Abbasi, A.H. Kokabi, Effect of vibration on machining and mechanical properties of AZ91 alloy during FSP: modeling and experiments, Int. J. Mater. Form. 14 (2021) 623–640, https://doi.org/10.1007/s12289-020-01551-2.
[32] B.R. Sunil, G.P.K. Reddy, H. Patle, R. Dumpala, Magnesium based surface metal matrix composites by friction stir processing, J. Magnes. Alloy. 4 (2016) 52–61, https://doi.org/10.1016/j.jma.2016.02.001.
[33] X. Zhao, X. Zeng, L. Yuan, J. Gandra, Q. Hayat, M. Bai, W.M. Rainforth, D. Guan, A novel approach for producing Mg-3Al-1Zn-0.2Mn alloy wire with a promising combination of strength and ductility using CoreFlowTM, Scr. Mater. 227 (2023) 115301, https://doi.org/10.1016/j.scriptamat.2023.115301.
[34] L. Yuan, X. Zeng, X. Zhao, Y. Xie, J. Gandra, D. Guan, Microstructure evolution and tensile behaviour of fine-grained 6082 Al wire with high ultimate strength and high work hardening by friction stir extrusion of bulk Al sheet, Mater. Sci. Eng. A 864 (2023) 144589, https://doi.org/10.1016/j.msea.2023.144589.
[35] L. Yuan, X. Zeng, X. Zhao, Y. Xie, J. Gandra, D. Guan, Dependence of microstructure evolution of novel CoreFlow^{TM} aluminium alloy wire on wire diameter, J. Mater. Res. Technol. 28 (2024) 2442–2454, https://doi.org/10.1016/j.jmrt.2023.12.177.
[36] D. Hardie, R.N. Parkins, Lattice spacing relationships in magnesium solid solutions, Philos. Mag. 4 (1959) 815–825, https://doi.org/10.1080/14786435908238237.
[37] G.C. Capitani, S. Di Pierro, G. Tempesta, The 6H-SiC structure model: Further refinement from SCXRD data from a terrestrial moissanite, Am. Mineral. 92 (2007) 403–407, https://doi.org/10.2138/am.2007.2346.
[38] J. Schindelin, I. Arganda-Carreras, E. Frise, V. Kaynig, M. Longair, T. Pietzsch, S. Preibisch, C. Rueden, S. Saalfeld, B. Schmid, J.-Y. Tinevez, D.J. White, V. Hartenstein, K. Eliceiri, P. Tomancak, A. Cardona, Fiji: an open-source platform for biological-image analysis, Nat. Methods 9 (2012) 676–682, https://doi.org/10.1038/nmeth.2019.
[39] A.S.T.M. Standards, Standard practice for heat treatment of magnesium alloys, ASTM Stand. 92 (2000) 1–7, https://doi.org/10.1520/B0661-12R20.
[40] Y. Zhu, J. Qin, J. Wang, P. Jin, Effect of sintering temperature on microstructure and mechanical properties of AZ91 magnesium alloy via spark plasma sintering, Adv. Eng. Mater. 24 (2022), https://doi.org/10.1002/adem.202100905.
[41] X. Hao, Z. Xu, C.M. Gourlay, Q. Li, Grain refinement of magnesium castings using recycled machining chips, Mater. Des. 244 (2024), https://doi.org/10.1016/j.matdes.2024.113138.
[42] J.D. Robson, D.T. Henry, B. Davis, Particle effects on recrystallization in magnesium–manganese alloys: particle-stimulated nucleation, Acta Mater. 57 (2009) 2739–2747, https://doi.org/10.1016/j.actamat.2009.02.032.
[43] A. Abdollahzadeh, B. Bagheri Vanani, A. Masoudi Morghmaleki, A. Ostovari Moghaddam, A.R. Eivani, Advancements in joining Al-Zn-TiC-Mg composites using friction stir welding process: influence of traverse speed, J. Compos. Mater. 58 (2024) 2757–2779, https://doi.org/10.1177/00219983241274502.
[44] A. Abdollahzadeh, B. Bagheri Vanani, H. Koohdar, A. Aboutalebi Babereh, M. Yeganeh, Multi-pass friction stir welding of Al–TiC–Zn–Mg composite: microstructure and mechanical characteristics, Metallogr. Microstruct. Anal. 13 (2024) 601–623, https://doi.org/10.1007/s13632-024-01117-7.
[45] A. Abdollahzadeh, B.B. Vanani, H. Koohdar, H.R. Jafarian, Influence of variation ambient system on dissimilar friction stir welding of Al Alloy to Mg Alloy by the addition of nanoparticles and interlayer, Met. Mater. Int. (2024) 2830–2852, https://doi.org/10.1007/s12540-024-01670-4.
[46] B. Bagheri Vanani, A. Abdollahzadeh, Fabrication of reinforced Al–Mg composite by TiC particles via FSW: microstructure and tribology study, J. Mater. Res. Technol. 30 (2024) 6787–6801, https://doi.org/10.1016/j.jmrt.2024.05.066.
[47] L. Wang, R. Lett, S. Felicelli, J. Berry, J. Jordon, D. Penrod, Microstructure and performance of four casting processes for magnesium Alloy AZ91, Int. J. Met. 5 (2011) 37–46, https://doi.org/10.1007/bf03355521.
[48] J.J. Petrovic, J.V. Milewski, D.L. Rohr, F.D. Gac, Tensile mechanical properties of SiC whiskers, J. Mater. Sci. 20 (1985) 1167–1177, https://doi.org/10.1007/bf01026310.
[49] Z. Zulkfli, N. Fatchurrohman, Advancement in friction stir processing on magnesium alloys, IOP Conf. Ser. Mater. Sci. Eng. 1092 (2021) 012006, https://doi.org/10.1088/1757-899x/1092/1/012006.
[50] K. Palanikumar, E. Natarajan, S. Suresh, D.G. Mohan, C. Prakash, K. Kaur, Prospects of friction stir processed Mg alloys and composites-reviews and suggestions, J. Mater. Res. Technol. 31 (2024) 971–997, https://doi.org/10.1016/j.jmrt.2024.06.087.
[51] Q. Zhang, X. Fu, G. Li, N. Chen, R. Shi, K. Chen, M. Wang, L. Peng, X. Hua, A. Shan, Macro-scale compositional inhomogeneity in friction stir processed Mg–Al–Zn cast alloy and its effect on mechanical property, Metall. Mater. Trans. A Phys. Metall. Mater. Sci. 55 (2024) 1550–1563, https://doi.org/10.1007/s11661-024-07343-6.
[52] P. Sagar, A. Handa, A comprehensive review of recent progress in fabrication of magnesium base composites by friction stir processing technique—A review, AIMS Mater. Sci. 7 (2020) 684–704, https://doi.org/10.3934/matersci.2020.5.684.
[53] G. Faraji, P. Asadi, Characterization of AZ91/alumina nanocomposite produced by FSP, Mater. Sci. Eng. A 528 (2011) 2431–2440, https://doi.org/10.1016/j.msea.2010.11.065.
[54] G. Faraji, M.M. Mashhadi, H.S. Kim, Microstructure inhomogeneity in ultra-fine grained bulk AZ91 produced by accumulative back extrusion (ABE), Mater. Sci. Eng. A 528 (2011) 4312–4317, https://doi.org/10.1016/j.msea.2011.02.075.
[55] F. Chai, F. Yan, W. Wang, Q. Lu, X. Fang, Microstructures and mechanical properties of AZ91 alloys prepared by multi-pass friction stir processing, J. Mater. Res. 33 (2018) 1789–1796, https://doi.org/10.1557/jmr.2018.98.
[56] P. Asadi, G. Faraji, M.K. Besharati, Producing of AZ91/SiC composite by friction stir processing (FSP), Int. J. Adv. Manuf. Technol. 51 (2010) 247–260, https://doi.org/10.1007/s00170-010-2600-z.
[57] A. Kumar, S. Kumar, N.K. Mukhopadhyay, A. Yadav, J. Winczek, Effect of SiC reinforcement and its variation on the mechanical characteristics of AZ91 composites, Materials (Basel). 13 (2020) 4913, https://doi.org/10.3390/ma13214913.
[58] W. Wang, P. Han, P. Peng, T. Zhang, Q. Liu, S.N. Yuan, L.Y. Huang, H.L. Yu, K. Qiao, K.S. Wang, Friction stir processing of magnesium alloys, A Review, Acta Metall. Sin. (English Lett.) 33 (2020) 43–57, https://doi.org/10.1007/s40195-019-00971-7.
[59] P. Asadi, M.K.B. Givi, K. Abrinia, M. Taherishargh, R. Salekrostam, Effects of SiC particle size and process parameters on the microstructure and hardness of AZ91/SiC composite layer fabricated by FSP, J. Mater. Eng. Perform. 20 (2011) 1554–1562, https://doi.org/10.1007/s11665-011-9855-x.
[60] J. Gu, L. Guo, B. Gan, Z. Bi, M. Song, Microstructure and mechanical properties of an MP159 alloy processed by torsional deformation and subsequent annealing, Mater. Sci. Eng. A 802 (2021), https://doi.org/10.1016/j.msea.2020.140676.
[61] C. María Abreu Fernández, R.A. Rey, M. Julia Cristóbal Ortega, D. Verdera, C.L. Vidal, Friction stir processing strategies to develop a surface composite layer on AA6061-T6, Mater. Manuf. Process. 33 (2018) 1133–1140. https://doi.org/10.1080/10426914.2017.1415447.
[62] H. He, G. Fan, F. Saba, Z. Tan, Z. Su, D. Xiong, Z. Li, Enhanced distribution and mechanical properties of high content nanoparticles reinforced metal matrix composite prepared by flake dispersion, Compos. Part B Eng. 252 (2023) 110514, https://doi.org/10.1016/j.compositesb.2023.110514.
[63] Q. Li, M. Zaiser, V. Koutsos, Carbon nanotube/epoxy resin composites using a block copolymer as a dispersing agent, Phys. Status Solidi 201 (2004) R89–R91, https://doi.org/10.1002/pssa.200409065.
[64] Q. Li, A. Viereckl, C.A. Rottmair, R.F. Singer, Improved processing of carbon nanotube/magnesium alloy composites, Compos. Sci. Technol. 69 (2009) 1193–1199, https://doi.org/10.1016/j.compscitech.2009.02.020.
[65] Y. Yang, X. Xiong, J. Chen, X. Peng, D. Chen, F. Pan, Research advances in magnesium and magnesium alloys worldwide in 2020, J. Magnes. Alloy. (2021), https://doi.org/10.1016/j.jma.2021.04.001.
[66] E. Georgantzia, M. Gkantou, G.S. Kamaris, Aluminium alloys as structural material: A review of research, Eng. Struct. 227 (2021) 111372, https://doi.org/10.1016/j.engstruct.2020.111372.
[67] R. Dong, W. Yang, P. Wu, M. Hussain, Z. Xiu, G. Wu, P. Wang, Microstructure characterization of SiC nanowires as reinforcements in composites, Mater. Charact. 103 (2015) 37–41, https://doi.org/10.1016/j.matchar.2015.03.013.